

# Performance of a Multi-anode Photomultiplier employing a weak electrostatic focusing system (Hamamatsu R8900 series)

Y. Kawasaki <sup>a</sup>, M. E. Bertaina <sup>a,\*</sup>,<sup>1</sup>, N. Sakaki <sup>b</sup>,  
H. M. Shimizu <sup>a</sup>, N. Inoue <sup>c</sup>, S. Hasegawa <sup>c</sup>, I. Ohtsu <sup>d</sup>,  
T. Adachi <sup>a</sup>, T. Ebisuzaki <sup>a</sup>, K. Hirota <sup>a</sup>, K. Ikeda <sup>a</sup>, F. Kajino <sup>e</sup>,  
T. Morishima <sup>a</sup>, M. Nagano <sup>f</sup>, M. Sato <sup>a</sup>, T. Sawabe <sup>e</sup>,  
T. Shibata <sup>b</sup>, T. Shinohara <sup>a</sup>, M. Takeda <sup>g</sup>, Y. Takizawa <sup>a</sup>,  
Y. Uchihori <sup>h</sup>, Y. Wada <sup>c</sup>

<sup>a</sup>*RIKEN, 2-1 Hirosawa, Wako, Saitama 351-0198, Japan*

<sup>b</sup>*Aoyama Gakuin University, 5-10-1 Fuchinobe Sagamihara, Kanagawa 229-8558,  
Japan*

<sup>c</sup>*Saitama University, 255 Shimo-Okubo Sakura-ku, Saitama 338-8570, Japan*

<sup>d</sup>*Electron Tube Division, Hamamatsu Photonics K.K., 314-5 Shimokanzo,  
Toyooka, Village Iwata-gun, Shizuoka 438-01, Japan*

<sup>e</sup>*Konan University, 8-9-1 Okamoto Higashi-nada, Kobe 658-8501, Japan*

<sup>f</sup>*Fukui University of Technology, 3-6-1 Gakuen, Fukui 910-8505, Japan*

<sup>g</sup>*Institute for Cosmic Ray Research, University of Tokyo, 5-1-5 Kashiwanoha,  
Kashiwa-shi, Chiba 277-8582, Japan*

<sup>h</sup>*National Institute of Radiological Sciences, 4-9-1 Anagawa, Inageku, Chiba-shi,  
263-8555, Japan*

---

## Abstract

We have developed a new type of multi-anode photomultiplier: Hamamatsu R8900-03 series. The main feature of R8900-03 series is a highly sensitive surface:  $\sim 83\%$  of the physical area. In this paper we report on the main characteristics of this new type of photomultiplier. R8900-03 series are suitable devices for experiments where high collection area and uniform detection efficiency are essential characteristics.

*Key words:* Multi-anode photomultiplier tube, Hamamatsu, R8900-03.

PACS: 42.79.Pw; 85.60.Gz

---

## 1 Introduction

Photomultipliers represent a standard device for detectors employed in many fields, nuclear and cosmic ray physics among others. In those fields, some experiments face the common problem of dealing with low beam intensities. Therefore maximization of the collection area, good and uniform response on the entire detector together with high spatial resolution are essential. Conventional multi-anode photomultipliers (MAPMT) offer a proper solution in terms of spatial resolution however they lack in sensitive area. This situation can be overcome by either improving existing photomultipliers or developing new type of photomultipliers such as flat panel or high quantum efficiency photomultipliers that employ semiconductor photo-cathodes.

In this paper we report on the development of already existing devices, in

---

\* Corresponding author. Tel./fax +81-48-467-9415

*Email address:* bertaina@stjcad.riken.jp (M. E. Bertaina).

<sup>1</sup> On leave of absence from Istituto Istruzione Superiore "Vallauri", Fossano, Italy

this case Hamamatsu R7600 series [1]. This choice is motivated by the fact that adapting already commercial MAPMT is the easiest and fastest solution together with the point that it is based on already existing suitable and reliable devices. Unfortunately R7600 series are characterized by a sensitive area of only  $\sim 45\%$  of the physical dimension that does not match with the requirements of high collection area and uniform response of the detector. The simplest solution is to enlarge the sensitive area of the photomultiplier. We have therefore developed a new MAPMT: Hamamatsu R8900 series. R8900 is a modified version of R7600 in which a grid has been inserted between the photo-cathode and the first dynode to electro-statically demagnify the photo-electron image onto the dynode. With this solution a sensitive area of  $\sim 83\%$  of the physical dimension has been obtained.

This paper reports on the main characteristics of R8900 MAPMT. Section 2 describes the design of the photomultiplier and test equipment. Sensitive area and the effect of focusing technique are reported in Section 3. Single photo-electron characteristics and MAPMT gain are described in Section 4. Section 5 is devoted to the study of the angular dependence of MAPMT response and the voltage dependence of gain. Detection efficiency and temperature dependence are described in Section 6 and results on the influence of an external magnetic field in Section 7. Finally Sections 8, 9 and 10 report on the radiation hardness, stability over time and mechanical stiffness studies. Conclusions are the object of the last session where, as an example, the possible suitability of this device for the EUSO mission and for the NOP project are briefly discussed.

## 2 Design of R8900 MAPMT and description of the calibration system

R8900 is a modified version of R7600. Therefore the fabrication process is common to both types of MAPMT. R8900 has a bi-alkali photo-cathode deposited on a UV-glass window 0.8 mm thick. Photo-electrons emitted from the photo-cathode are weakly focused into the acceptance of a 12-stage stack of metal channel dynodes. The distinctive characteristics of R8900 is a weakly focusing system obtained by means of an electrode placed between photo-cathode and first dynode whose effect is to concentrate photo-electrons produced on almost the entire photo-cathode onto the sensitive region of the first dynode. This feature can make a MAPMT sensitive to photons even near the edge of the photo-cathode. R8900 have been so far fabricated in the M16 ( $4 \times 4$ ), M25 ( $5 \times 5$ ) and M36 ( $6 \times 6$ ) anode formats (see Figures 1 and 2). The physical dimension of R8900 is  $\sim 26 \times 26 \times 27$  mm<sup>3</sup> and the weight  $\sim 27$  gr, values slightly varying according to the anode format.

The schematic drawing of the MAPMT calibration system is shown in Fig-

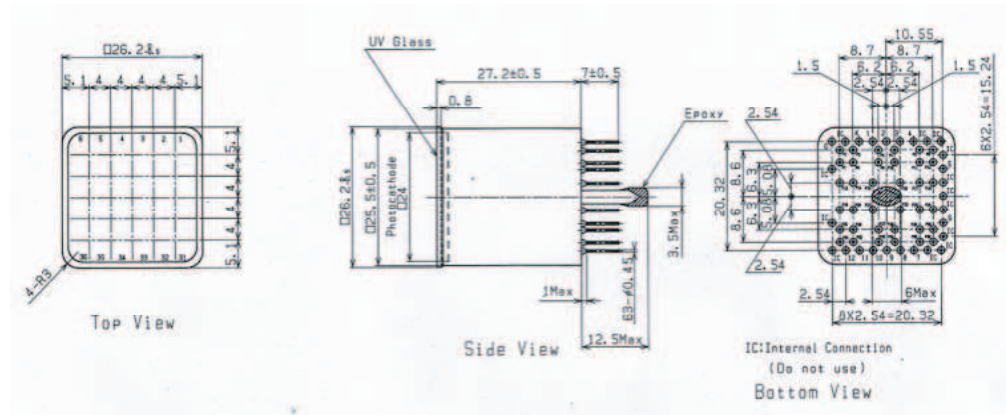


Fig. 1.

ure 3. A UV LED (NICHIA NSHU590E, with peak wavelength of 370 nm



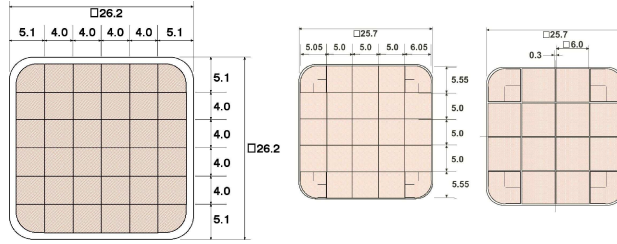
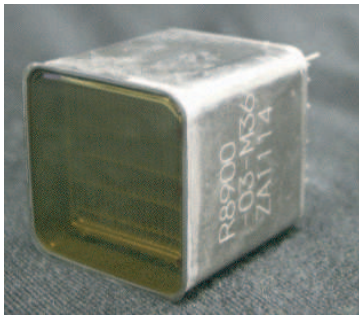


Fig. 2.

and spectrum FWHM of 12 nm) was settled at one edge of a cylinder of 20 cm length and 3 cm diameter, mounted on a  $xyz\theta$  4-axis stage. In order to reduce the width of the light beam two pinholes were used. The first one, 3 mm size, was placed in the middle of the cylinder; the second one, 100  $\mu\text{m}$  diameter, was attached at the other edge of the cylinder. The measured beam intensity distribution in this conditions is shown in Figure 4. The FWHM size of the beam is  $\sim 60 \mu\text{m}$ . MAPMT and the 4-axis stage were installed

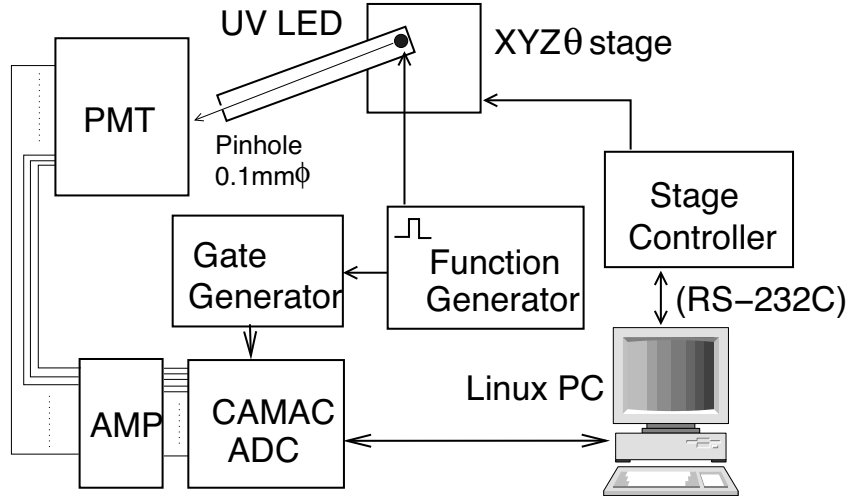


Fig. 3.

in a black box of  $1 \times 1 \times 1 \text{ m}^3$  size. The axes were controlled by a stage controller (SURUGA SEIKI D70) and a Linux PC was used to communicate with the stage controller via RS-232C, the precision of the positioning of the stage being  $< 10 \mu\text{m}$ . The area of  $\sim 30 \text{ mm} \times 30 \text{ mm}$ , which is larger than

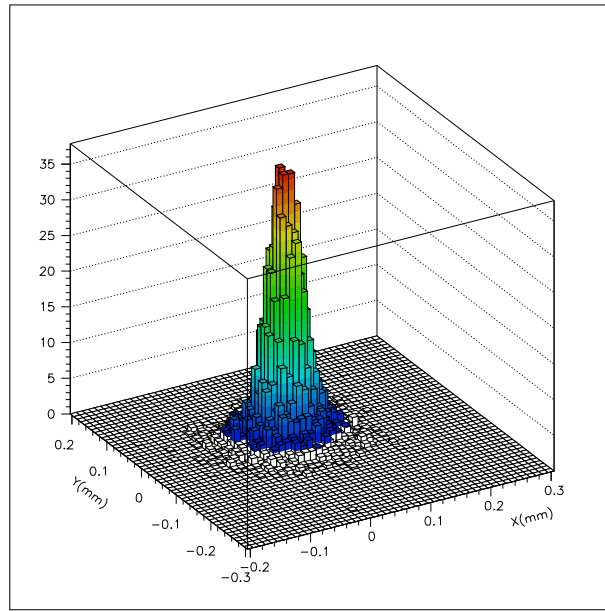


Fig. 4.

the photo-cathode area, was scanned with a step of 0.1 mm to 1.0 mm, depending on the level of precision required in the measurement, the position resolution of the stage being 2  $\mu\text{m}$ . The absolute position of the beam was determined so that the output distribution fitted to the anode format. The anode outputs of the MAPMT was amplified by ten and converted to digital values by a CAMAC ADC (REPIC ADC-022). CAMAC crate controller (TOYO-TECHNICA CC7700) and Linux PC communicated with each other by way of the PCI interface card for CC7700. The MAPMT was powered by means of a REPIC power supply (model RPH-030) at High Voltage (H.V.) of -900 V and with termination impedance of the signal cable of 50  $\Omega$  if no other value is expressly mentioned. As an example the voltage divider used for M36 is reported in Figure 5. UV LED was powered by a pulse generator with rate 1 kHz. Typical estimated number of photons in the measurement of sensitivity maps is  $\sim 4000$  using a 300 ns pulse width and a 100  $\mu\text{m}$  diameter pinhole, value slightly varying with MAPMT gain. Regarding figures shown in the rest of the paper, if no other information is supplied, the position of pixel 1 has to

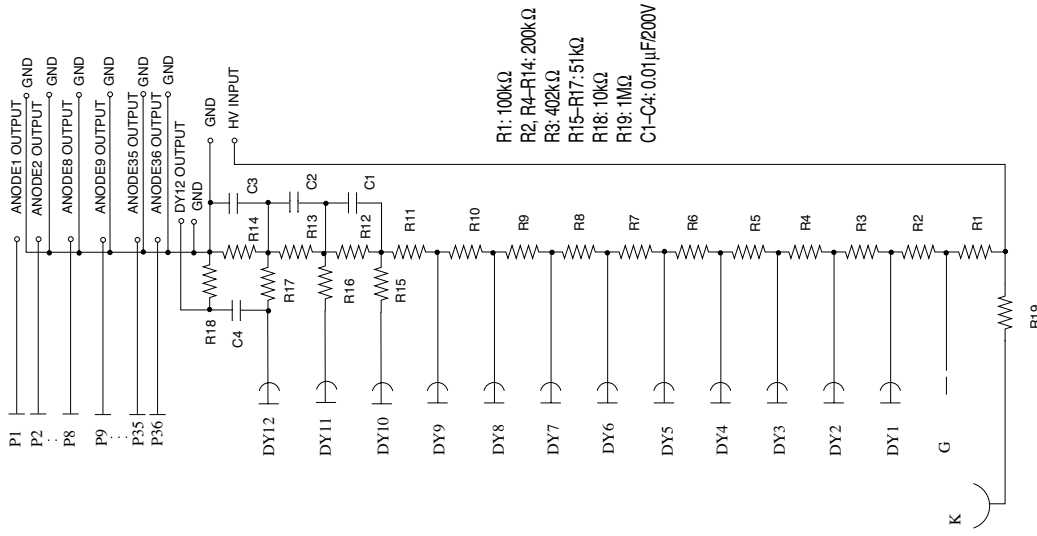


Fig. 5.

be assumed at the bottom-right corner and pixel  $N$  ( $N = 16, 25, 36$  depending on the anode format) at the top-left corner of the plot.

### 3 Sensitive area of R8900 and effect of focusing technique

By using the apparatus described in the previous paragraph sensitivity maps of R8900 were measured and compared to R5900 series. By sake of completeness R5900 and R7600 series differ only slightly in that the latter lacks an external mounting flange. Hamamatsu Photonics replaced R5900 model with R7600.

In measuring sensitivity maps,  $g_i(x, y)$  was defined as the output of  $i$ -th channel of the MAPMT and  $(x, y)$  was the position where the LED illuminated the photo-cathode. Figure 6 (left) shows the total sensitivity map of R8900-M16, that is  $g(x, y) = \sum_{i=1}^N g_i(x, y)$  where  $N$  is the number of pixels ( $N=16$  for R8900-M16) while Figure 7 shows sensitivity maps ( $g_i(x, y)$ ) of single pixels. Panels of Figure 6 show the relative output level  $g(x, y)$  to the maximum

signal detected during the measurement. Right side of Figure 6 also shows

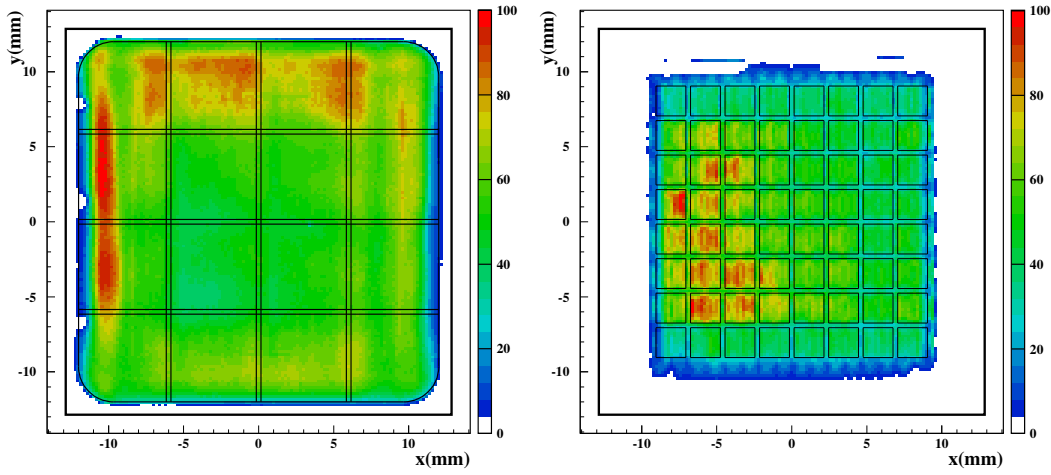


Fig. 6.

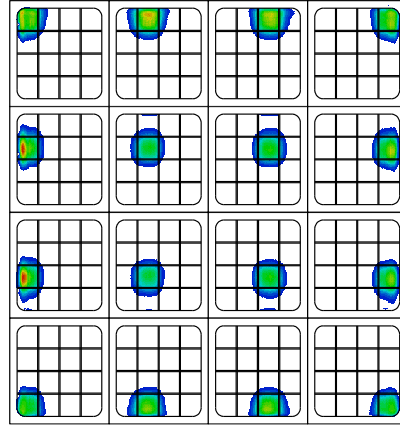


Fig. 7.

the sensitivity map of R5900-M64. We defined the sensitive area, as the ratio, expressed as a percentage, between the area where photo-electrons were collected from (colored area in Figure 6) and a squared area (rounded black square) whose side corresponds to the MAPMT physical size, metal package included ( $25.7 \times 25.7 \text{ mm}^2$ ). The sensitive area of R8900-M16 fills on the whole photo-cathode even at the edges and areas between pixels. Uniformity

becomes better on the whole region. This electron focusing feature improves sensitive area up to  $\sim 83\%$  compared to  $\sim 45\%$  for the R5900 one. Insensitive area still remains, due mainly to the packaging material. If necessary, it could be easily recovered by adding an optical adapter on the photo-cathode in order to increase the sensitive area ratio up to or over 90%.

Figures 8 and 9 show respectively sensitivity and single anode maps for R8900-M36. The sensitivity area of M36 is similar to M16 and extends on the whole surface of the photo-cathode. However, by looking at the single anode maps, less uniformity is noticeable between inner and border pixels at this stage of development. Especially pixels at the corners have a sensitive area about half of the inner ones. Moreover a halo structure appears in the outer pixels. For sake of completeness sensitivity maps of M25 show the same lack of uniformity between inner and border pixels but no halo structures are observed.

In order to quantify such lack of uniformity among pixels we defined the

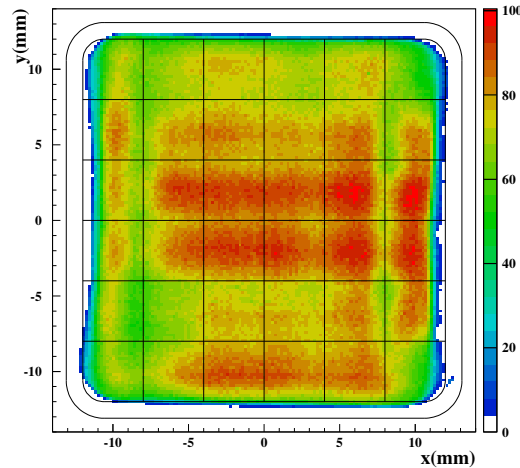


Fig. 8.

uniformity ratio parameter in the following way. First of all the center  $(\bar{x}_i, \bar{y}_i)$  of pixel  $i$ -th was determined. As a second step the output  $(g_i^j)$  of the same pixel in all the  $j$  positions of the beam in an area of  $12 \times 12 \text{ mm}^2$  around the

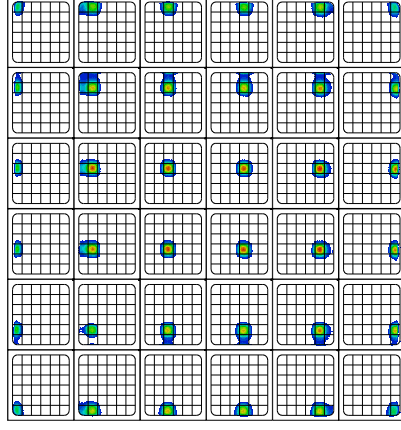


Fig. 9.

center of the pixel was summed up together and a total output per pixel ( $G_i$ ) obtained:

$$G_i = \sum_j g_i^j \quad (1)$$

$$|x_i^j - \bar{x}_i| \leq 6mm \wedge |y_i^j - \bar{y}_i| \leq 6mm.$$

As each pixel has on average a size of about  $6 \times 6 \text{ mm}^2$  for M16,  $5 \times 5 \text{ mm}^2$  for M25 and  $4 \times 4 \text{ mm}^2$  for M36, the area previously defined is sufficiently wide to include all the significant points but not extremely big in order to reduce the effect of background signals exceeding the subtracted pedestal. Finally the uniformity ratio was defined as  $u.r. = \max(G_i)/\min(G_i)$ .

With such definition two different effects are included: a) the difference in spatial uniformity of the pixels, that means the variation of the output sensitivity with respect to the photo-cathode position due either to the photo-cathode uniformity or to the electron multiplier (dynode section) uniformity; b) the different photo-cathode area to which each pixel is sensitive. As the M25 had been delivered in much higher quantity, the uniformity ratio was evaluated using a high statistics (50 MAPMT). The average u.r. is 4.0 (r.m.s. = 0.7).

A similar analysis was conducted on M36 and M16 types with a more limited statistics. M36 provided a similar result, while M16 showed better uniformity: u.r.  $\sim 2.0$ .

The halo structure observed on the M36 (9) is a clear sign of cross-talk between pixels. Cross-talk between pixels on the MAPMT occurs by two different mechanisms: a) primary photo-electrons being multiplied in the wrong pixel's dynode chain ('optical cross-talk'); b) electrons leaking from one dynode chain to another near the bottom of the chain resulting in a small fraction of the injected charge moving to the wrong dynode channel or anode ('electrical cross-talk'). Even though we don't distinguish the origin in our analysis, by looking at the shape of this cross-talk, it is clear that most of the effect is 'optical cross-talk', mainly due the precision of the electrostatic focusing system to focus photo-electrons on the correct dynode chain. A common way to measure cross-talk consists in irradiating a light spot in the center of one pixel and measuring the output of the near-by pixels respect to the signal detected by the irradiated one. Cross-talk of pixel  $n$  ( $cr(n)$ ) is defined in the following as the ratio between the average value among the signals ( $g(m)$ ) collected by the nearby pixels ( $m$ ) and the signal collected by that in the center ( $n$ ) when light is illuminating the center of pixel  $n$ . In formula:

$$cr(n) = \frac{\sum_{m=n-7}^{n-5} g(m) + g(n-1) + g(n+1) + \sum_{m=n+5}^{n+7} g(m)}{k \times g(n)} \quad (2)$$

where  $k = 8$  for an inner pixel. For edge and corner pixels the sum indicated in formula 2 is computed only on the existing pixels, therefore  $k = 5$  for border pixels and  $k = 3$  for corner ones. In our measurement the cylinder was located at the center of the pixel, the spot size being  $\sim 100 \mu\text{m}$  and the distance of the

cylinder from the MAPMT window  $\sim 2$  mm. Using this method the average cross-talk measured by one near-by pixel is  $\sim 1\%$  for M16 (see Figure 10),  $\sim 2\%$  for M25 and  $\sim 7\%$  for M36. The higher value obtained for M36 reflects the halo structures observed in the pixels at the edges. Figure 11 shows the typical cross-talk of M36. A clear difference between inner and edge pixels is observed, while the central ones have a reasonable behavior, those at the edges and especially at the corners have a worse performance. The same analysis was performed using signals at single photo-electron level and similar results were obtained [2].

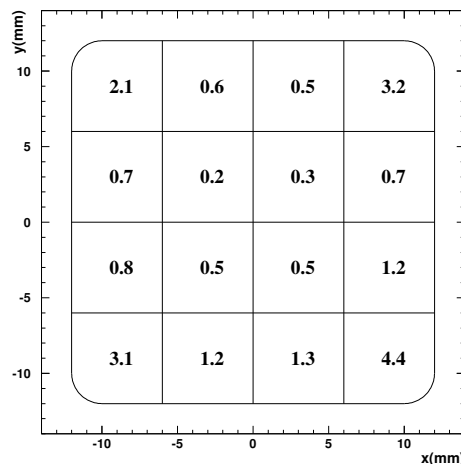


Fig. 10.

#### 4 Single photo-electron characteristics and MAPMT gain

In order to measure the signal corresponding to one photo-electron, an optical filter was placed inside the cylinder of the calibration system near the pin-hole, the output signal being approximately 1 photo-electron per pulse. The pinhole was located around the center of the pixel where, according to the



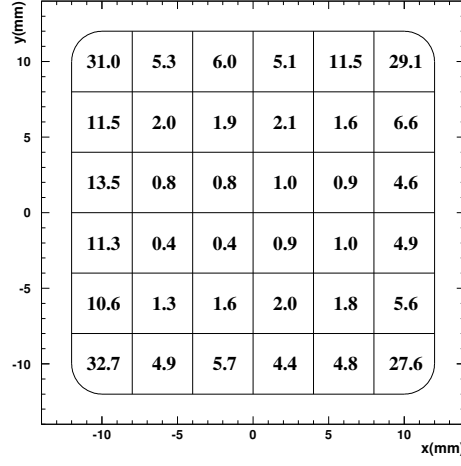


Fig. 11.

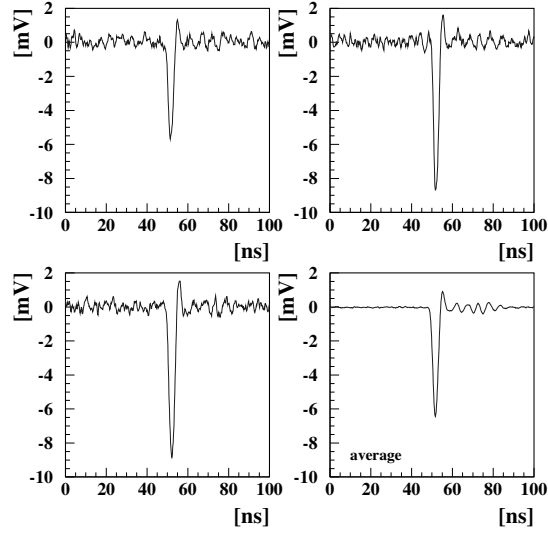


Fig. 12.

sensitivity maps, the collection efficiency is expected to be high. Figure 12 shows sample waveforms of signals from a pixel of R8900-M25 with gain  $\sim 2 \times 10^6$ . Characteristics of such waveforms are: pulse height  $\sim 6.4$  mV, rise and fall time (10% to 90%)  $\sim 2$  ns, width (FWHM)  $\sim 3$  ns. Since after pulse was not observed above the noise level, it is estimated to be smaller than 1/10 of the main pulse. We can observe ringing effect at the tail of the pulse. As this effect might affect measurements employing photon counting method where

fast response and clear pulse shape are required conditions, a new version of high voltage divider is under development.

Average gain of several M25 and M36 MAPMT was estimated. Gain of each pixel was computed through a Gaussian fit of the peak of the single photo-electron spectrum. A systematic uncertainty on the order of  $\sim 10\%$  was considered for the correct estimation of the gain. It included uncertainties in the amplification chain, correct determination of the pedestal and single photo-electron peak, ringing effect of the signals integrated with the ADC (see Figure 12). Gain of R8900-M25 varies between  $\sim 3 \times 10^5$  and  $\sim 6 \times 10^6$ , the average value being  $2.2 \times 10^6$ . Gain of M36 varies between  $\sim 2 \times 10^6$  and  $\sim 12 \times 10^6$ , the average value being  $4.8 \times 10^6$ . The distribution of the relative variation of gain among pixels of the same MAPMT is on the order of 20%.

Single photo-electron spectra of few M16 was also measured in self triggering mode. Typical gain is  $3.1 \div 5.5 \times 10^6$  at H.V. = -900 V.

Figure 13 (left) reports single photo-electron spectra measured for R8900-M36 at H.V. = -900 V. Single photo-electron peaks, whose characteristics are re-

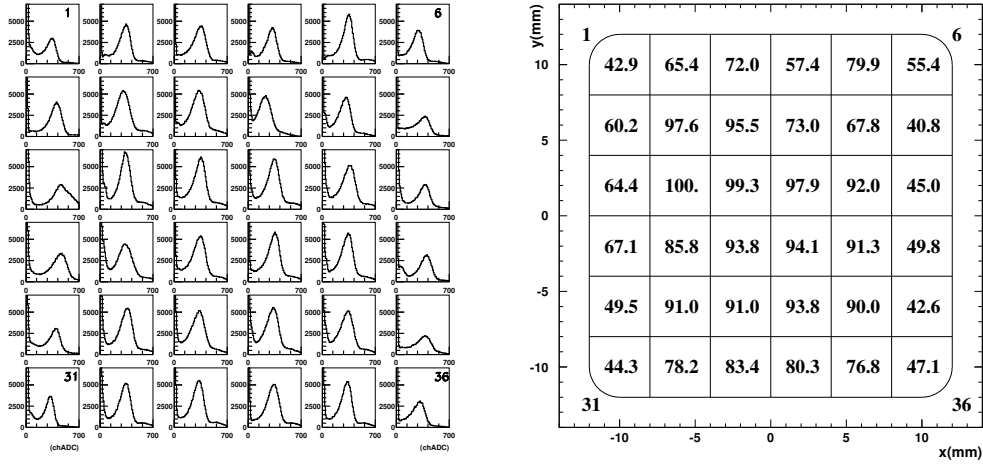


Fig. 13.

ported in Table 1, are well defined. MAPMT average gain is  $5.4 \times 10^6$  and

r.m.s.  $0.7 \times 10^6$ . The average Peak to Valley ratio (P/V) is 4.2 and r.m.s. = 0.8. The average single photo-electron peak resolution, is 55% and r.m.s. = 9%. As the spectra of M36 were obtained by triggering on the LED pulser with light pointing at the center of the pixel, we should expect about the same number of signals above the pedestal for all pixels. However pixels on the first and last columns show a lower number of events. This effect is summarized on the right side of Figure 13 where the percentage of events above 1/3 of the single photo-electron threshold, computed relatively to the pixel with the highest number of events, is reported. The number of signals above 1/3 of the single photo-electron peak vary in a factor of 2.3. This fact is related to the difference in Detection Efficiency (D.E.) and more specifically to the Collection Efficiency (C.E.) already observed on single anode maps. A more detailed discussion on the D.E. is object of Section 6.

## **5 Angular dependence of sensitivity, voltage dependence and linearity of gain**

Dependence of sensitivity on the inclined incidence of photons on the photo-cathode was measured by means of 50 R8900-M25 MAPMT. Top panel of Figure 14 shows the average dependence of relative outputs of 50 MAPMT on the angle  $\theta$  between incident light and photo-cathode plane. Distributions of 50 MAPMT responses at four different  $\theta$  are shown in lower panels. The average relative output is higher than 0.87 up to  $60^\circ$ ; r.m.s. of each distribution varies between 1 ÷ 2%. Similar results were obtained measuring the angular dependence for M36 either in terms of sensitivity maps and D.E. maps.

High Voltage dependence was studied with R8900-M36. MAPMT was scanned

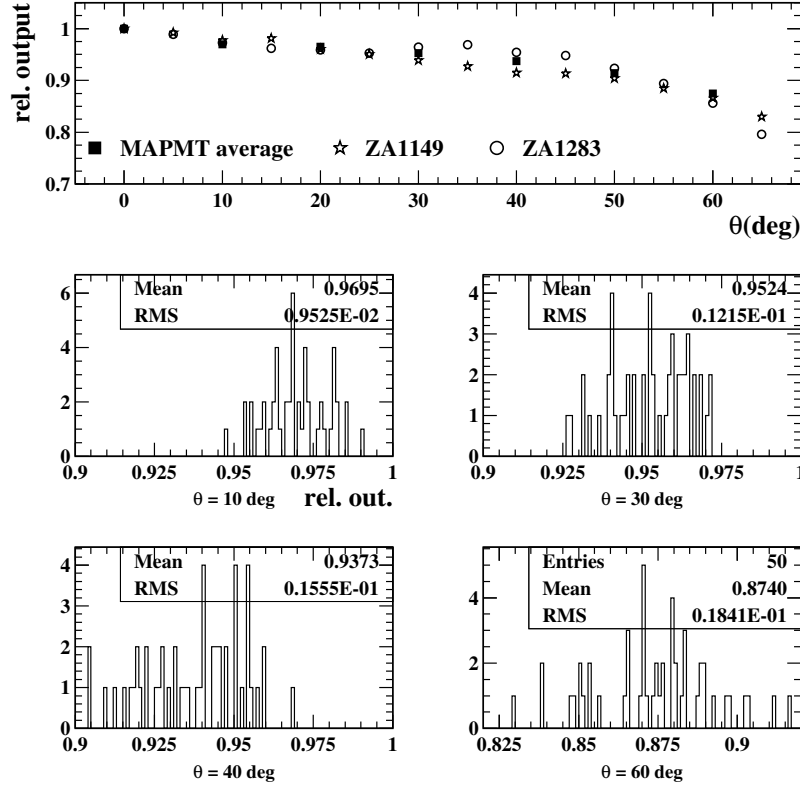


Fig. 14.

using a signal equivalent to about  $\sim 30$  photo-electrons and measurement repeated at different supplied powers between H.V. of -550 V and -1000 V. Measurements between -700 V and -1000 V were then performed using a signal equivalent to  $\sim 1$  photo-electron, a more suitable condition for experiments employing the photon counting method. Figure 15 shows the average dependence in single photo-electron mode obtained averaging 36 sets of data, one for each pixel for a typical MAPMT. In this figure the two measurements are normalized at -900 V. Voltage dependence of gain can be parametrized on the whole scale by a relationship of the form  $G = a \times HV^b$ . In our measurement  $\log(a) = -21.21 \pm 0.59$  and  $b = 9.42 \pm 0.20$ . In the region -700 V  $\div$  -950 V experimental points differ by less than 10% from the fitted function.

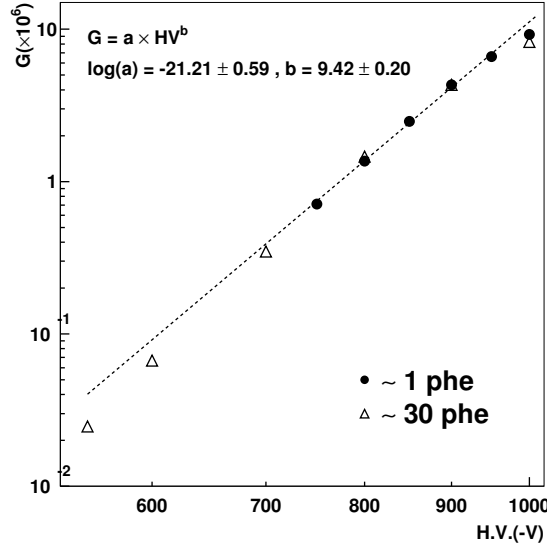


Fig. 15.

## 6 Signal-to-noise ratio, detection efficiency and temperature dependence

Single photon counting method is a suitable technique for experiments dealing with very low input signals, on the order of few photo-electrons per pixels, as it prevents systematic errors from gain drift. In this case a threshold level has to be fixed in the single photo-electron spectrum in order to optimize the signal-to-noise ratio (S/N) and stabilize the counting rate against gain fluctuations. The threshold setting ( $V_{th}$ ) of 1/3 single photo-electron peak ( $V_0$ ) is around the valley of the single photo-electron distribution, giving an appropriate value (see Figure 18). Figure 16 shows the dark current at the threshold level of  $V_{th}/V_0 = 1/3$  as a function of temperature for M16. The measured temperatures are 10 °C, 20 °C, 25 °C, 30 °C, 35 °C and 50 °C. The S/N measurement was computed at room temperature on two M36, obtaining similar results: 19.49 counts/sec, r.m.s. = 15.30 counts/sec (ZA1969); 10.10 counts/sec, r.m.s. = 9.12 counts/sec (ZA1968). On average pixels at the edges

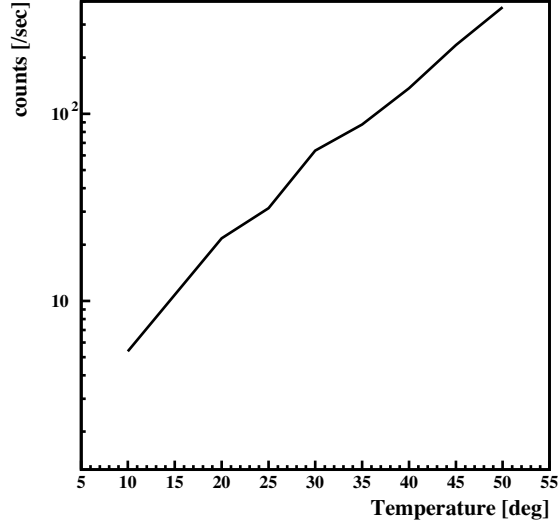


Fig. 16.

show a lower dark count rate compared to the inner ones.

In order to estimate the photon counting rate it is important to know the common effect of quantum efficiency (Q.E.) and collection efficiency (C.E.) of MAPMT, called detection efficiency (D.E. = Q.E.  $\times$  C.E.) hereafter. We measured D.E. of M16, M25 and M36 with our system. D.E. was estimated by comparing the single photo-electron distribution with the reference PMT (H7195PX) whose absolute calibration is known. For both H7195PX and R8900, the detected counts ( $N_{p.e.}$ ) above 1/3 single photo-electron peak were measured, and Q.E.  $\times$  C.E. for R8900 calculated using the following relation:

$$\left. \frac{N_{p.e.}}{Q.E. \times C.E.} \right|_{H7195PX} = \left. \frac{N_{p.e.}}{Q.E. \times C.E.} \right|_{R8900} \quad (3)$$

Value of D.E. measured for M25 and M16 is  $\sim 0.14$  consistent with the typical value of  $Q.E. \times C.E. = 0.2 \times 0.7 = 0.14$  that can be assumed from literature. Regarding M36 we measured the D.E. map of 9 MAPMT (see Figure 17). The apparatus used in this measurement was slightly different from that shown in

Figure 3. Signals from the anodes were discriminated by a N-TM 405 (Tech-

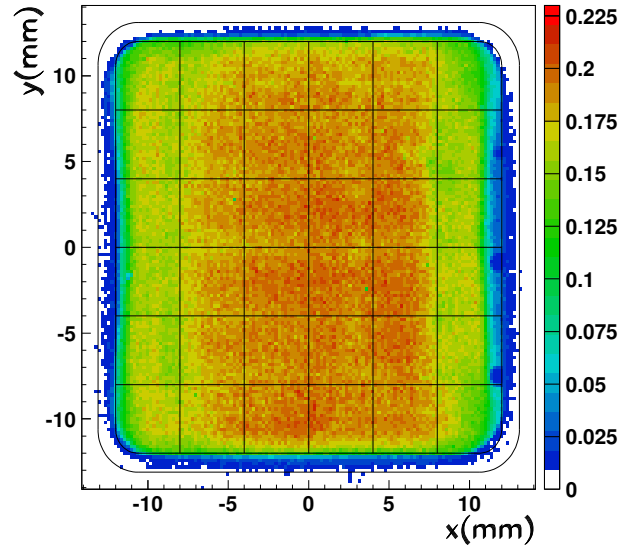


Fig. 17.

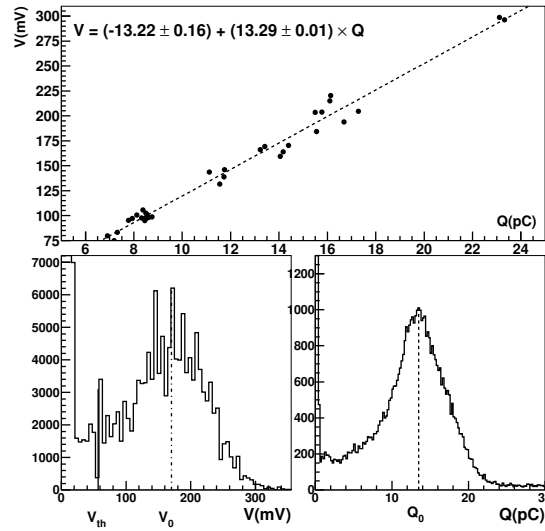


Fig. 18.

noland Corp.) 8 ch discriminator (low threshold -10 mV) and then counted by a scaler (REPIC RPC-160) together with the number of pulses provided to the LED. Thresholds of the discriminator were set at  $V_{th} = 1/3 V_0$  of the single photo-electron peak. As the location of  $V_{th}$  is in the valley between

pedestal and signal peak (see Figure 18), a 20% shift of the threshold varies the total number of counts by less than 5%. We can assume this value as an indication of the systematic uncertainty of our measurement. As a result of the measurement of 9 MAPMT we obtained an average D.E. =  $(15.8 \pm 0.6)\%$ . This value is higher compared to M25 and M16 because M36 are the result of a further development made in order to increase quantum efficiency (Q.E. being about 24% at  $\lambda = 370$  nm from preliminary measurements on few MAPMT). Figure 19 (left) reports the D.E. pixel by pixel (average of 9 MAPMT). The r.m.s. of the distribution is 2.3%. The ratio between the pixel with maximum and minimum D.E. is 1.59. If we assume that Q.E. is 24% homogeneous on the entire photo-cathode, the difference in D.E. corresponds to a difference in C.E. Right side of Figure 19 reports the C.E. deduced under this assumption. An improvement of C.E. at the edges is under development to get a better and more uniform C.E. over the entire photo-cathode.

Temperature dependence of D.E. in the region  $-20\text{ }^{\circ}\text{C} \div +50\text{ }^{\circ}\text{C}$  was studied

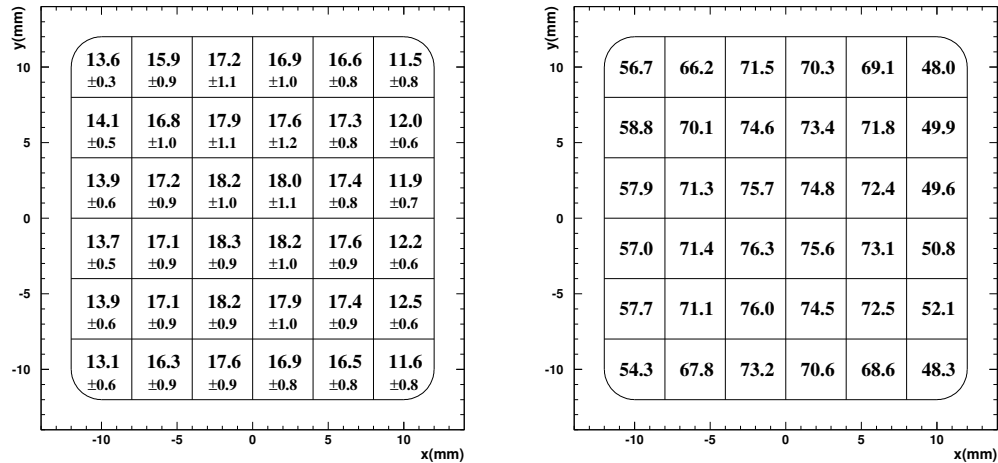


Fig. 19.

using M16 by means of a YAP pulser (YAlOe:Ce scintillator +<sup>241</sup>Am, 50 Bq, peak wavelength 370 nm, decay time 28 ns). D.E. at 25 °C was measured as



explained above, and the relative variation with temperature was measured with the YAP pulser, the temperature dependence of the YAP pulser being  $-0.4\%/^{\circ}\text{C}$ . The YAP pulser was mounted on the MAPMT surface with a mask to limit the light illuminated into a central channel. The injected number of photons was estimated to be about 1000. The charge distribution for this photon injection was taken with a gate window 200 ns. The peak ADC channel was interpreted to be proportional to D.E.  $\times$  Gain. The temperature dependence of the gain was measured from the single photo-electron distribution and no dependence was found. As a result, the peak of the distribution for the YAP pulser was interpreted to be proportional to D.E. The relation between D.E. and temperature is expressed by  $\Delta D.E./\Delta T/D.E. = -0.37\%/^{\circ}\text{C}$ . The temperature dependence for another MAPMT is  $-0.33\%/^{\circ}\text{C}$ . These values are consistent with typical values reported in literature [3] for a bi-alkali photo-cathode in the region of wavelengths  $300 \div 400$  nm.

## 7 Influence of external magnetic field

Because of their focusing feature, R8900 MAPMT are more sensitive to the influence of an external magnetic field compared to R7600 series, therefore the effect of magnetic field on the R8900-M36 response was studied. The error on the magnetic field including measurement uncertainty and field inhomogeneity is  $\sim 0.2$  mT. The following coordinate system was defined (Figure 20). The x-axis is parallel to the photo-cathode and perpendicular to the first dynode structure. The y-axis is parallel to the first dynode and z-axis is perpendicular to the photo-cathode. The direction is defined so that the youngest pixel aligns along the x-axis at largest y-values.

Figure 21 shows the magnetic field dependence of R8900-M36. The output

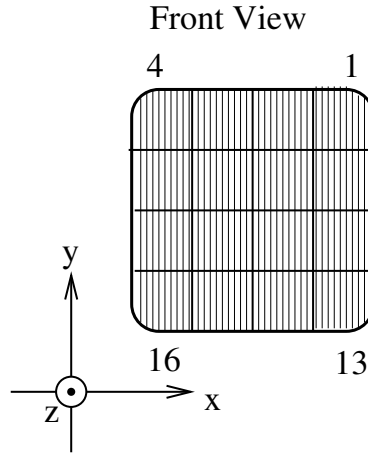


Fig. 20.

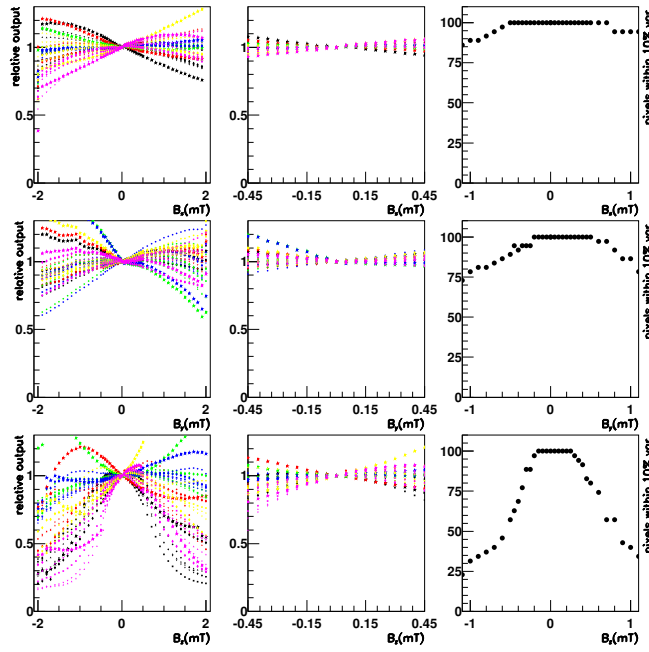


Fig. 21.

is normalized to 1 at  $|B| = 0$ . The sensitivity of MAPMT depends mostly on the magnetic field along z-axis (see bottom plot of left column). The central column shows a detailed behavior of MAPMT for low applied magnetic fields.

The right column indicates the percentage of pixels whose gain variation due to the external magnetic field is  $\leq 10\%$  compared to the case of no magnetic field. No pixel shows a variation higher than 10% for  $B_{x,y,z}$  lower than 0.2 mT. Same measurement was performed on M16. Results were similar to those of M36 and hence a difference of influence of external magnetic field due to the pixel size was not observed.

## 8 Influence of radiation

Either in space applications or in experiments at accelerator sites, photo-multipliers are subject to radiation stress. The influence of radiation on the MAPMT is dominated by the degradation of the entrance window transparency, causing color centers and indirectly changing the electrochemical characteristics of the photo-cathodes. On the other hand, influence on cathode sensitivity and electron amplification is negligibly small compared with the transparency degradation. Transparency is degraded by 10% beyond  $1.4 \times 10^5$  R for gamma-rays in the MeV region [3]. We checked the transparency degradation for 70 MeV proton beam using a cyclotron at National Institute of Radiological Sciences (NIRS), Japan [4]. We used a beam profile of 10 cm diameter, the fluctuation in beam intensity being  $< 20\%$ . The total beam fluence was controlled by the exposure time. In this measurement 8 glasses were irradiated and their transparency measured by an optical spectrometer before and after irradiation. Figure 22 shows that no significant decrease of relative transparency is observed for exposure doses  $< 10$  krad for all three wavelengths. Transparency decreases to 95% beyond 100 krad.

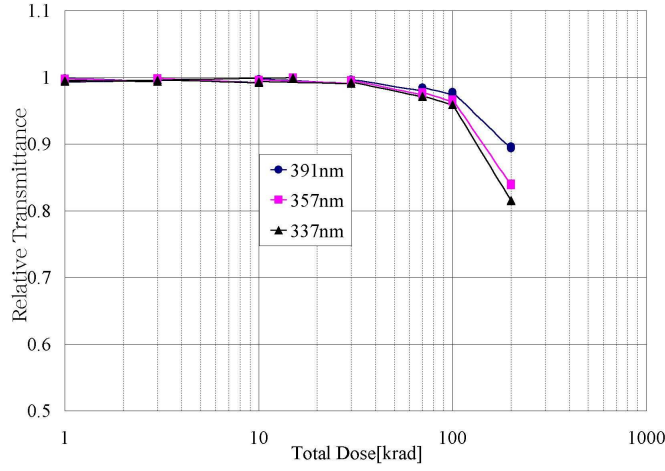


Fig. 22.

## 9 Aging effect

We checked the temporal stability of the MAPMT (M36) gain under highly intense incident light [5]. We employed a system similar to that described in Section 2 to which a programmable H.V. supply was added. LED was substituted with NSHU550 (peak wavelength of 370 nm and spectrum FWHM of 10 nm). It has a much wider directivity, i.e. light intensity in a direction of  $30^\circ$  from light axis is 90% of that on the light axis ( $0^\circ$ ).

The LED was set in front of the MAPMT surface at a distance of 6 cm and non uniformity of light intensity on the MAPMT surface is expected to be  $< 10\%$  according to the LED directivity and the geometry of the experiment. Total charge from each pixel was measured by ADC within a gate time of 800 ns, synchronized with LED drive signal. Voltage of -850 V was supplied to the MAPMT corresponding to a gain of  $2 \times 10^6$ . In this measurement MAPMT was illuminated constantly for 6 ms with repetition rate of 100 Hz. The number of photons per gate time was estimated to be 163 photons/pixel/800ns on average for all pixels from a charge measurement of each pixel, taking into

account MAPMT gain and detection efficiency. As LED was flashed with a drive signal of 6 ms width, the total number of photons was estimated as  $1.2 \times 10^6$  per pixel in a flash. This experiment was done in a total time duration of 31766 minutes equivalent to a total accumulated incident photon amount of  $2.3 \times 10^{14}$  photons/pixel. A typical ADC count variation during

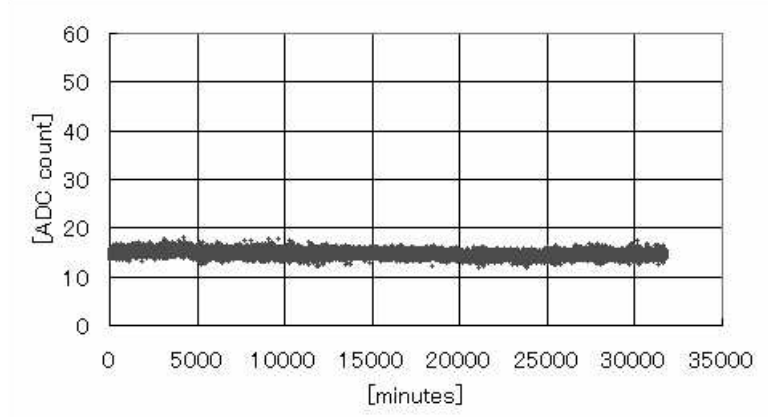


Fig. 23.

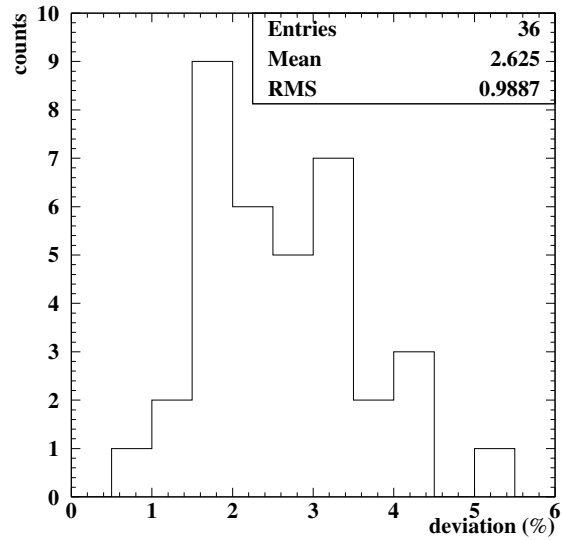


Fig. 24.

light illumination is shown in Figure 23. Time variability of the average ADC counts for each pixel was calculated, and deviation from the overall average

to minimum ADC counts in this time duration is reported in Figure 24. All pixels show a gain variation in time less than 6% in this experiment, the average being 2.6%, which shows that no apparent negative characteristics, caused by highly intense incident light, was found.

## 10 Mechanical stiffness

R7600 MAPMT have been already successfully employed in space applications [6]. In such type of experiments detectors are transported in orbit by means of space vehicles therefore they should be stiff enough to bear strong vibrations occurring in launching phase. Therefore we checked the critical vibrational limit of M25 and M36 MAPMT. In the vibration test of M25 we used a vibration generator EMIC F-300BN (model 9003-FN) while for M36 vibration generator EMIC F-1000BDH. The frequency profile is the random vibration environment reported in Table 2. Duration of vibration was 2 minutes. Since tests were made in the order of increasing acceleration, accumulated damage of each MAPMT has to be considered. Figure 25, as an example, reports

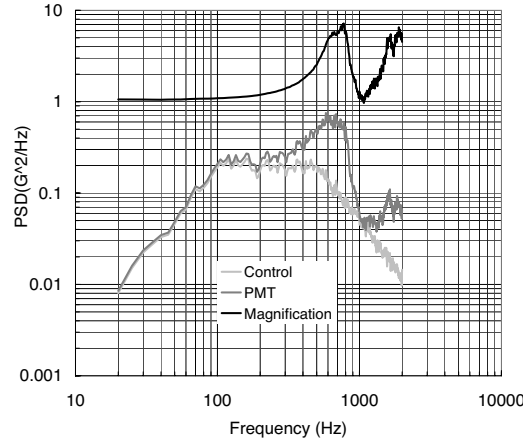


Fig. 25.

frequency profile during vibration test of M36 [7]. Figure 26 shows the relative

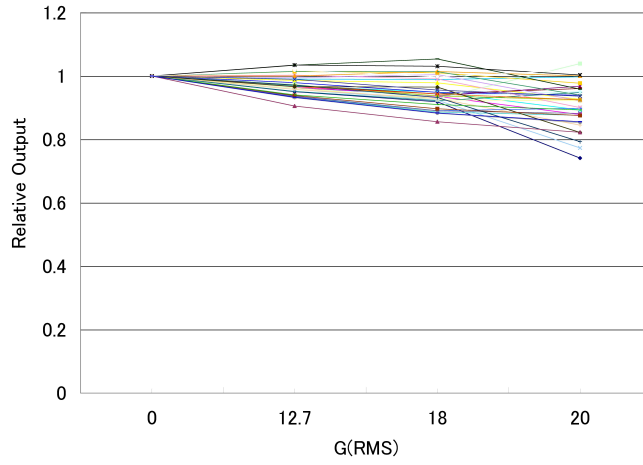


Fig. 26.

output as a function of the average acceleration for M36. M36 output is stable (variations  $< 5\%$ ) up to  $12.7\text{ g}$  (r.m.s.) and breaking point exceeds  $20\text{ g}$ . Same test repeated with M25 showed that R8900-M25 endures random vibrations up to  $20.4\text{ g}$  (r.m.s.) with a relative output decrease on average  $< 10\%$ .

## 11 Conclusions

We have developed a new type of MAPMT (Hamamatsu R8900 series) in the formats of 16, 25 and 36 pixels featuring a weak focusing electrostatic system. The main result of this development is the increase of the sensitive area to  $\sim 83\%$  of the physical dimension of the MAPMT. This result is very important for experiments dealing with low beam intensities, in this sense two possible applications are suggested in the following. We carried out an extensive series of measurements to check the characteristics and performance of this type of MAPMT. Main results obtained so far are summarized in Table 3.

One possible candidate to employ this new type of MAPMT is the Extreme Universe Space Observatory (EUSO) telescope [8]. EUSO is a space mission

for the observation of atmospheric fluorescence and Čerenkov photons accompanying the extensive air showers induced by extremely high energy cosmic rays (EHECRs) around  $10^{20}$  eV. EUSO telescope is a refractive wide angle telescope ( $60^\circ$ ) to look down the atmosphere of about 400 km diameter. It is scheduled to be installed on the External Payload Facility of the Columbus module of the European Space Agency in the International Space Station and observe EHECRs during its 3÷5 years mission period. It comprises of a pair of double-sided curved Fresnel lenses with a curved focal surface and the related electronics. The focal surface detector [9] is a closely packed mosaic of MAPMT approximating the curved focal surface. Near-ultraviolet photons are selectively delivered on to the focal surface detector by employing an optical filter in the optics or on the top of the detector. A signal rate on the order of 5 photo-electrons/ $\mu$ s from air showers of  $10^{20}$  eV at maximum development is expected on the focal surface [10]. Because EUSO detects faint signals localized in space and time on the focal surface, the photo-detector should satisfy several severe requirements such as single photon sensitivity in the 330÷400 nm wavelength range, with a good and uniform detection efficiency, fast response, on the order of  $\Delta t \sim 10$  ns and a spatial resolution of few mm, low noise and good signal-to-noise ratio, with small cross-talk and after-pulse rate. It must cover the focal surface with a sensitive area as large as possible and it must be compatible with space mission requirements such as low mass, low power consumption, mechanical and radiation hardness, low sensitivity to magnetic fields and high reliability and operating stability over a period of a few years. The characteristics of R8900 series, as reported in Table 3, seem therefore to fit quite well EUSO requirements.

A second project that might take advantage of this development is the Neutron



Optics Project (NOP) [11]. This project is intended to use very low energy neutron beams (from very cold to thermal neutrons:  $10^{-6}$  eV  $\div$  0.1 eV) to study organic molecules and bio-molecules, based on the fact that very low energy neutrons are a very effective probe to study light elements such as hydrogen. Unfortunately the effective utilization of these neutron beams is strongly limited by the small number of neutron sources and by low beam intensity. Objective of this project is therefore to increase the efficiency of neutron beams maximizing their output by means of improving the focusing optics, such as reflective (super-mirrors) or refractive optics (compound refractive optics or magnetic optics) [11]. Neutron beams are finally detected by imaging detectors employing devices such as micro-strip chambers, or  $^3\text{He}$  cryogenic chambers, photomultipliers with high collection area or high detection efficiency, semiconductor detectors [12]. In this sense R8900 series could be very precious in these detectors for imaging purposes having a high collection area and good spatial resolution.

## 12 Acknowledgments

This study was partially supported by the "Ground-based Research Announcement for Space Utilization" promoted by Japan Space Forum, by Special Coordination Funds for promoting the Ministry of Education, Culture, Sports, Science and Technology of the Japanese Government and by JSPS (Japan Society for Promotion of Science) Grants-in-Aid for Scientific Research #14340084. M.E.B. expresses his gratitude to JSPS for providing him a Postdoctoral Fellowship for Foreign Researchers to accomplish part of the present studies at RIKEN.

## References

- [1] Hamamatsu Photonics K.K., Multi-anode Photomultiplier tube R7600 series data sheet, <http://jp.hamamatsu.com>.
- [2] Bertaina M. et al., Int. Journal of Mod. Phys. A 20 N.29 (2005) 6872.
- [3] Hamamatsu Photonics K.K., PMT Handbook Ver.2, Hamamatsu (1998).
- [4] Uchihori Y. et al., Proc. 29<sup>th</sup> ICRC, HE 1.5 (2005).
- [5] Inoue N. et al., Proc. 29<sup>th</sup> ICRC, HE 1.5 (2005).
- [6] Alpat B., Nucl. Phys. B (Proc. Suppl.) 85 (2000) 15.
- [7] Kawasaki Y. et al., Proc. 29<sup>th</sup> ICRC, HE 1.5 (2005).
- [8] Catalano O., Il Nuovo Cimento C 24 (2001) 445.
- [9] Ameri M. et al., Nucl. Instr. Meth. A 504 (2003) 99.
- [10] Shimizu H. M. et al., AIP Conf. Proc. 566 (2001) 381.
- [11] Shimizu H. M. et al., Physica B 311 (2002) 123.
- [12] Sakai K. et al., Physica B 350 (2004) e841.

### 13 Figure captions

Fig. 1. Mechanical drawing of R8900-03-M36.

Fig. 2. Photograph of R8900-03-M36 (left) and design view of R8900-03-M36, M25 and M16 (right). Units are expressed in mm.

Fig. 3. Schematic drawing of MAPMT calibration system (see text for explanation).

Fig. 4. Intensity profile of the UV light beam used in the measurements (units mm on both x and y axis).

Fig. 5. R8900-M36 voltage divider.

Fig. 6. Typical sensitivity maps of R8900-M16 (left) and R5900-M64 (right). The black rounded square corresponds to the area where sensitivity was computed, same size for both MAPMT. Panels on the right of each plot show the relative output level  $g(x, y)$  to the maximum signal detected during the measurement (see text for details).

Fig. 7. Typical single anode maps for R8900-M16. Each box (16 in total) reports the sensitive region of each pixel. Color scale is the same as in Fig. 6.

Fig. 8. Typical sensitivity map of R8900-M36. Panel on the right shows the relative output level  $g(x, y)$  to the maximum signal detected during the measurement (see text for details).

Fig. 9. Typical single anode maps of R8900-M36. Color scale is the same as in Fig. 8.

Fig.10. Cross-talk level (%) pixel by pixel for M16 shown in Fig. 7.

Fig.11. Cross-talk level (%) pixel by pixel for M36 shown in Fig. 9.

Fig.12. Three sampled waveforms of R8900-M25 for a signal equivalent to 1 photo-electron and average one obtained averaging 128 waveforms (lower right).

Fig.13. Single photo-electron spectra of a typical R8900-M36 (gain  $\sim 5.4 \times 10^6$ ) on the left (values on the x axis are expressed in ADC channels). On the right side, percentage of events above 1/3 of the single photo-electron peak relatively to the pixel with the highest number of events as obtained from the spectra reported on the left.

Fig.14. Average angular dependence of relative output for R8900-M25 (top). The angular dependence of two specific MAPMT is indicated together with the average one (statistics 50 MAPMT). Distributions of MAPMT response at different angles are displayed in the 4 bottom plots. The output at  $0^\circ$  is assumed to be 1.

Fig.15. Typical High Voltage dependence of gain for M36 measured using a signal equivalent to 1 photo-electron (circles) or equivalent to  $\sim 30$  photo-electrons (triangles).

Fig.16. Dark count rate above the single photo-electron peak as a function of temperature.

Fig.17. Detection efficiency map of a typical M36. Absolute values of D.E. are reported in the right panel.

Fig.18. Relation between the single photo-electron peaks obtained in charge mode (pC) and peak height (mV) mode (top). Single photo-electron peak measured in peak height (left) and charge (right) modes (bottom). Threshold ( $V_{th}$ ) at 1/3 of the single photo-electron in peak height mode is also indicated.

Fig.19. Left: average detection efficiency, pixel by pixel, for R8900-M36 (statistics 9 MAPMT). Right: collection efficiency, pixel by pixel, for R8900-M36. These values were obtained from left-side figure assuming an average Q.E. of 24%.

Fig.20. The coordinate system used for the orientation of magnetic field.

Fig.21. Variation of relative gain as a function of magnetic field strength (units mT for  $B_x$  top,  $B_y$  central,  $B_z$  bottom rows) is shown in left and central columns (central column is a detail of left one). Different markers show different pixels. The ratios of number of pixels whose signal vary less than 10% relative to no magnetic field as a function of magnetic field strength is shown in the right column.

Fig.22. Relative transmittance of glass window as a function of the total dose.

Fig.23. An example of ADC time variation during aging test.

Fig.24. Distribution of the average decrease of gain after the aging test for all 36 pixels.

Fig.25. Typical vibration profile of M36 during test with vibration axis perpendicular to the photo-cathode.

Fig.26. Relative output of each pixel of M36 as a function of the average acceleration on the axis perpendicular to the photo-cathode after vibration tests.

pixel	G	P/V	res(%)	pixel	G	P/V	res(%)	pixel	G	P/V	res(%)
1	5.3	2.7	47	13	6.9	5.1	63	25	6.1	3.0	46
2	5.3	4.5	53	14	5.3	5.3	50	26	5.6	4.4	53
3	5.4	4.4	55	15	5.5	4.3	51	27	5.2	3.8	66
4	4.9	4.8	54	16	5.4	4.6	55	28	5.1	4.1	61
5	5.5	5.7	46	17	5.7	3.6	55	29	5.2	3.7	65
6	4.5	3.9	62	18	5.9	4.0	48	30	5.9	2.8	55
7	6.3	6.0	44	19	7.2	4.1	46	31	5.0	4.1	41
8	4.8	4.0	58	20	5.2	3.0	63	32	5.3	4.3	53
9	5.1	3.9	64	21	5.4	3.9	58	33	5.1	4.8	52
10	3.4	2.6	94	22	5.5	4.6	51	34	5.3	5.0	53
11	4.9	3.9	55	23	5.3	4.9	53	35	5.1	5.2	52
12	5.9	2.6	53	24	6.2	4.6	48	36	4.8	3.7	68

Table 1

Pixel's gain (G, in unit  $10^6$ ), Peak to Valley ratio (P/V) and single photo-electron resolution (res) obtained at H.V.= -900 V for M36 shown in Figure 13.

frequency range	vibration profile
20 Hz ÷ 100 Hz	$\sim +6.00$ dB/oct
100 Hz ÷ 500 Hz	$0.20 \text{ } g^2/\text{Hz}$ (for 12.7 $g$ r.m.s.)
500 Hz ÷ 2000 Hz	$-6.00$ dB/oct

Table 2

Characteristics of frequency profile used in the vibration test.



MAPMT parameters	R8900 characteristics
Window	0.8 mm UV glass
Casing	KOVAR metal
Size	$\sim 26 \times 26 \times 27 \text{ mm}^3$
Pixel size	4 mm (M36) - 6 mm (M16)
Weight	$\sim 27 \text{ gr}$
Photo-cathode	bi-alkali
Dynode type	metal channel, 12 stages
Spectral response	260 to 530 nm (Q.E. $\geq 10\%$ )
Peak Sensitive Wavelength	370 nm
Anode dark current	$\leq 0.1 \text{ nA}$ per pixel
Maximum HV	1000 V (neg.)
Gain at -900 V	$\sim 3 \times 10^6$ (typ.)
Pulse height (@ $5 \times 10^6$ )	$\sim 16 \text{ mV}$
Pulse rise-fall time(10%÷90%)	$\sim 2 \text{ ns}$
Pulse Width (FWHM)	$\sim 3 \text{ ns}$

Table 3

Summary of the characteristics of R8900 MAPMT.

MAPMT parameters	R8900 characteristics
Non Linearity	$\leq 10\%$ from -700 V to -950 V.
Pixel uniformity	1:4 (M25, M36), 1:2 (M16)
Cross-talk	$\sim 1\%$ (M16), $\sim 2\%$ (M25), $\sim 7\%$ (M36)
Dark current counts	$\sim 10 \div 20$ Hz
(room temperature)	
Detection Efficiency	14% (M25, M16)
	15.8%, r.m.s.=2.3% (M36)
Temp. dependence of D.E.	-0.37%/°C
Angular response	$\geq 90\%$ (rel. to 0°) up to 50°
External magnetic field	$\leq 10\%$ rel. output @ B < 0.2 mT
Radiation hardness	5% loss of window transp. @ 100 krad
Aging effect	< 6% @ $2.3 \times 10^{14}$ photons/pixel
Mechanical stiffness	< 5% gain var. @ 12.7 g (r.m.s.)
	break point $\geq 20$ g

Table 3

Continuation of Table 3.

## 14 Black and white figures for print version

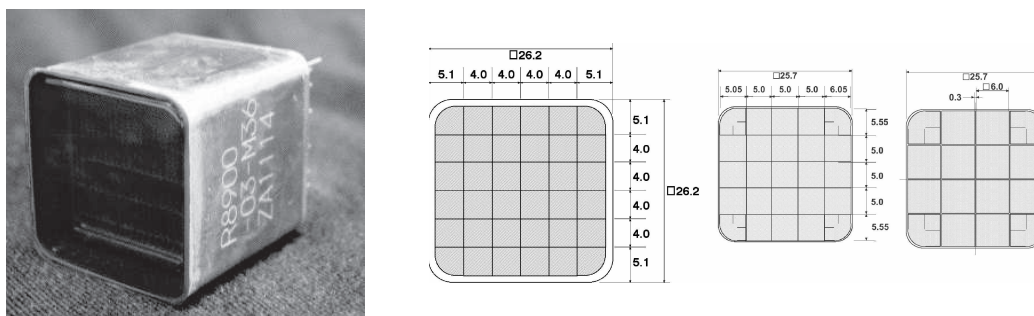


Fig. 27. This figure substitutes fig. 2 in print version.

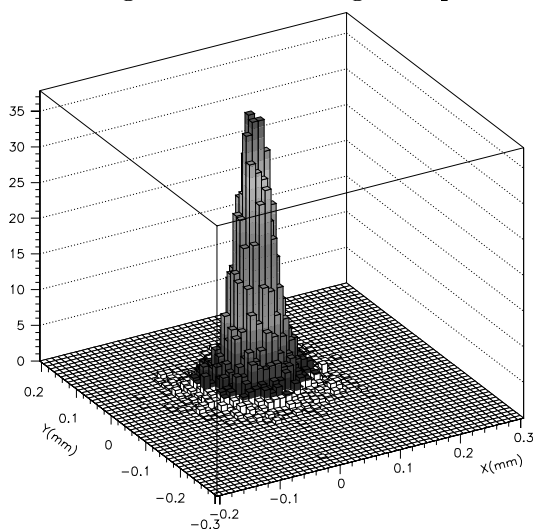


Fig. 28. This figure substitutes fig. 4 in print version.

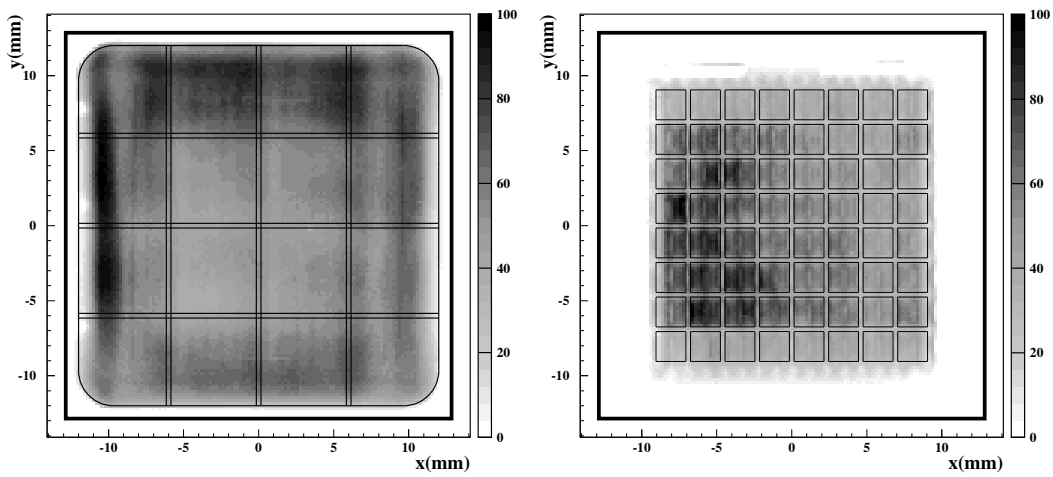


Fig. 29. This figure substitutes fig. 6 in print version.

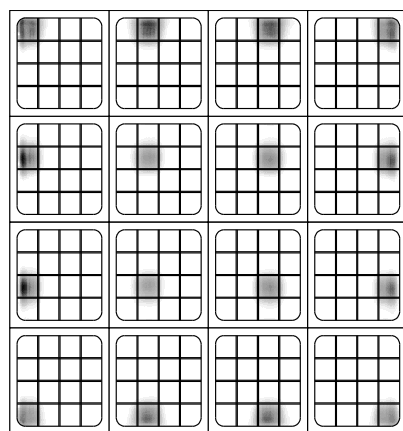


Fig. 30. This figure substitutes fig. 7 in print version.

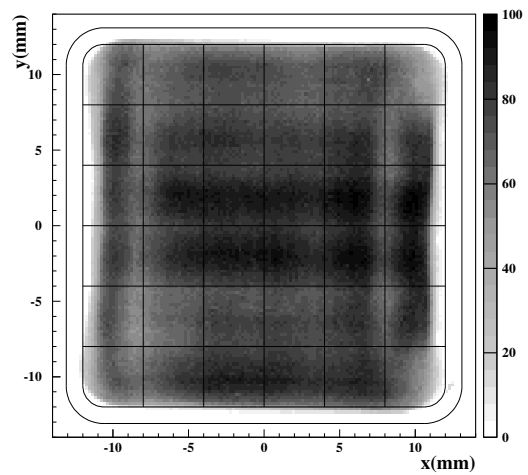


Fig. 31. This figure substitutes fig. 8 in print version.

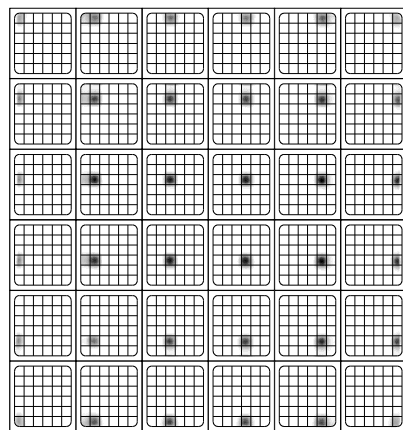


Fig. 32. This figure substitutes fig. 9 in print version.

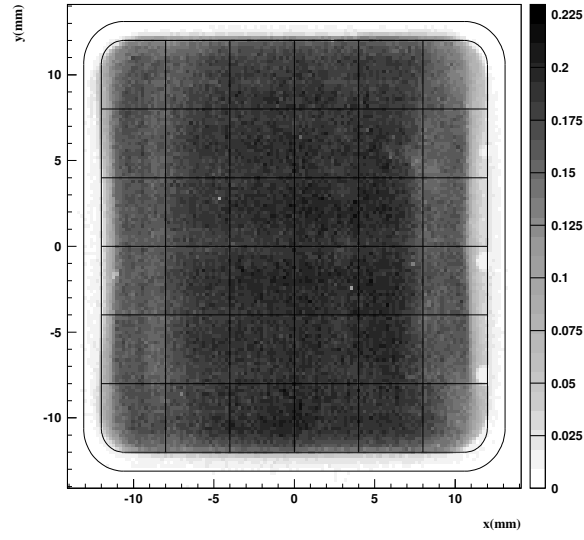


Fig. 33. This figure substitutes fig. 17 in print version.

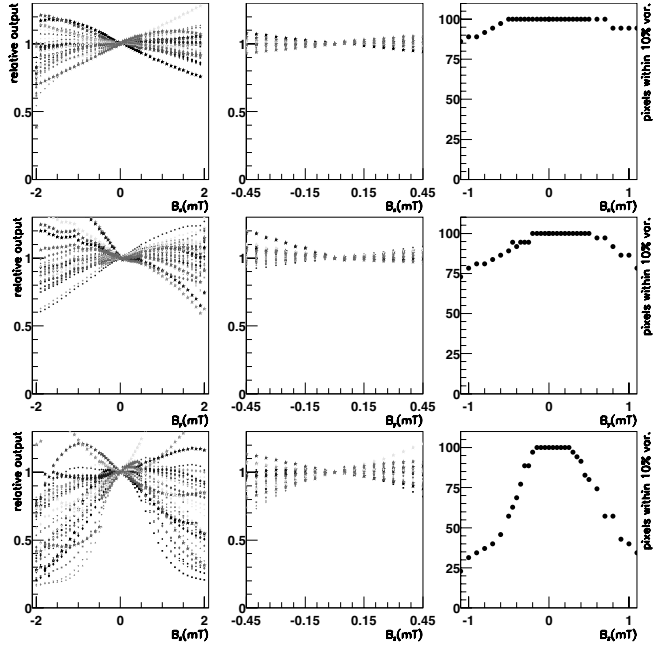


Fig. 34. This figure substitutes fig. 21 in print version.

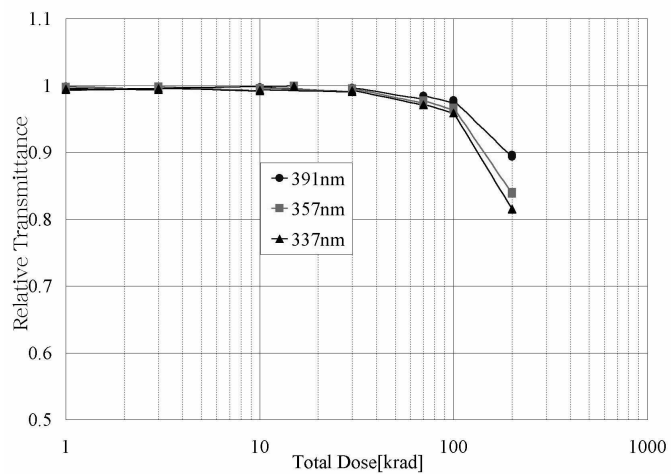


Fig. 35. This figure substitutes fig. 22 in print version.

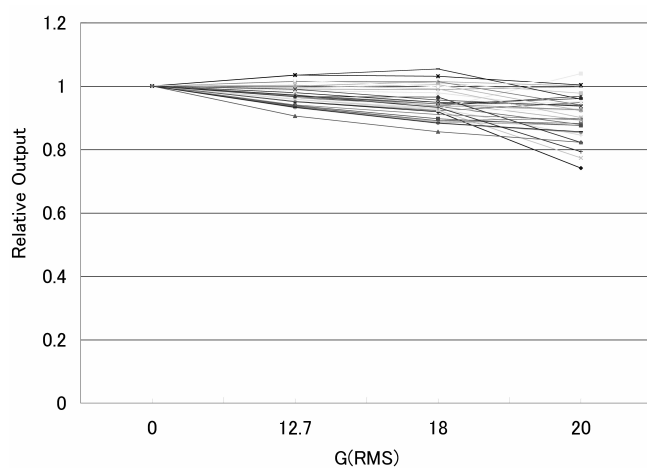


Fig. 36. This figure substitutes fig. 26 in print version.